Available online at www.sciencedirect.com

SCIENCE @ DIRECT®

International Journal of Heat and Mass Transfer 47 (2004) 4075–4087

International Journal of HEAT and MASS TRANSFER

www.elsevier.com/locate/ijhmt

A numerical study on the fluid flow and heat transfer around a circular cylinder in an aligned magnetic field

H.S. Yoon [a], H.H. Chun [a], M.Y. Ha [b,*], H.G. Lee [c]

[a] *Advanced Ship Engineering Research Center, Pusan National University San 30, Chang Jeon Dong, Kum Jeong Gu, Pusan 609-735, South Korea*
[b] *School of Mechanical Engineering, Pusan National University San 30, Chang Jeon Dong, Kum Jeong Gu, Pusan 609-735, South Korea*
[c] *LG Electronics Co., Air Conditioning Division, 76 Sungsan, Changwon, South Korea*

Received 12 March 2004; received in revised form 12 May 2004
Available online 2 July 2004

Abstract

The present study numerically investigates two-dimensional laminar fluid flow and heat transfer past a circular cylinder in an aligned magnetic field using the spectral method to insure the accuracy of results. For the purpose of controlling vortex shedding and heat transfer, numerical simulations to calculate the fluid flow and heat transfer past a circular cylinder are performed for different Reynolds numbers of 100 and 200 and for different Prandtl numbers of 0.02 (liquid metal), 0.7 (air) and 7 (water) in the range of $0 \leqslant N \leqslant 10$, where N is the Stuart number (interaction parameter) which is the ratio of electromagnetic force to inertia force. The present study reports the detailed information of flow and thermal quantities on the cylinder surface at different Stuart numbers. As the intensity of applied magnetic fields increases, the vortex shedding formed in the wake becomes weaker and the oscillating amplitude of lift coefficient decreases. The flow and thermal fields become the steady state if the Stuart number is greater than the critical value, which depends on the Reynolds number. Thus the drag and lift coefficients and Nusselt number representing the fluid flow and heat transfer characteristics also vary as a function of Stuart number.

1. Introduction

The phenomenon of flow separation, bluff body wake and prediction of heat transfer from a cylinder have been intensely studied for a long time because of their fundamental significance in flow physics and their practical importance in aerodynamic and heat transfer applications. Braza et al. [1]; Mittal and Balalchandar, [2]; Williamson [3]. The generation and evolution of vortical structures in the wake region have a big effect on the drag, heat transfer, flow-induced vibration and noise problems. Thus, to control the vortical structure in the wake properly is very important in the aspect of real engineering application.

Various methods were suggested to control vortex shedding in the wake, using endplate Stansby [4], splitter plate Roshko [5]; Unal and Rockwell [6]; Gerrard [7]; Kwon and Choi [8], inhomogeneous inlet flow Gaster [9]; Gerich and Eckelmann [10], blockage Shair et al. [11], base bleed Wood [12]; Bearman [13]; Schumm et al. [14], second cylinder in the wake Strykowski and Sreenivasan [15], speaker Roussopoulos [16], suction and blowing slots Park et al. [17] and rotation or oscillation of the cylinder Tokumaru and Dimotakis [18]; Beak and Sung [19]; Kang et al. [20], Choi et al. [21]. Kwon and Choi [8] summarized well the characteristics of these methods to the control the vortex shedding.

Recently, there have been some researches to apply the magnetic fields to control the vortical structure in the

---

[*] Corresponding author. Tel.: +82-51-510-2440; fax: +82-51-512-9835.
E-mail address: myha@pusan.ac.kr (M.Y. Ha).

0017-9310/$ - see front matter © 2004 Elsevier Ltd. All rights reserved.
doi:10.1016/j.ijheatmasstransfer.2004.05.015

Nomenclature

B_0	external magnetic field
C_{Dp}	pressure drag coefficient
C_{Df}	friction drag coefficient
C_D	drag coefficient ($= C_{Dp} + C_{Df}$)
C_{Lp}	pressure lift coefficient
C_{Lf}	friction lift coefficient
C_L	lift coefficient ($= C_{Lp} + C_{Lf}$)
C_P	pressure coefficient
D	cylinder diameter
f_r, f_θ	Lorentz forces in radial and circumferential direction
n	normal direction to the wall
N	Stuart number or interaction parameter
Nu	local Nusselt number
$\langle Nu \rangle$	surface-averaged Nusselt number
$\langle \overline{Nu} \rangle$	time and surface-averaged Nusselt number
p	dimensionless pressure
Pr	Prandtl number
r, θ	dimensionless radial and circumferential direction
Ra	Rayleigh number
St	Strouhal number
t	dimensionless time
t_p	period of time integration
T	dimensionless temperature
T_s	cylinder surface temperature
T_∞	free stream temperature
u_r, u_θ	dimensionless radial and circumferential velocity
U_∞	free stream velocity
W	cylinder surface
x, y	Cartesian coordinates

Greek symbols

α	thermal diffusivity
β	thermal expansion coefficient
ρ	density
σ	electric conductivity
ν	kinematic viscosity
ω_w	wall vorticity

Subscripts/superscripts

cr	critical value
max	maximum
min	minimum
*	dimensional value
–	time-averaged quantity

wake. They investigated the effect of magnetic fields on the flow structure past a cylinder. Lahjomri et al. [22] carried out an experimental study and showed that an aligned magnetic field leaded to the suppression of vortex shedding. Shatrov et al. [23] and Mutschke et al. [24–26] investigated the flow instability in the wake in the presence of magnetic fields from their numerical studies. They carried out the stability analysis using the numerical simulation techniques for the time-dependent two- and three-dimensional flow. Depending on the magnitude of applied magnetic fields in the two-dimensional flow region, the vortex shedding can be suppressed or eliminated and as a result the flow becomes stabilized.

Most of previous researches to study the effect of magnetic fields on the flow past a cylinder are mainly to investigate the change of flow structure in the whole flow field. However, their studies did not give the detail quantitative information about the flow variables such as drag and lift coefficients, Strouhal number, pressure coefficient and wall vorticity on the cylinder surface in the presence of magnetic fields. Studies on the heat transfer from a cylinder in the presence of magnetic fields are also little.

In the present study, we investigated the effects of magnetic fields on the fluid flow and heat transfer past a cylinder. We obtained the numerical solutions for unsteady two-dimensional governing equation for the flow and heat transfer using the accurate spectral method. We calculated the drag and lift coefficients, Strouhal number, pressure coefficient, wall vorticity and Nusselt number as a function of the magnitude of applied magnetic fields.

2. Governing equations

Fig. 1 shows the computational domain and coordinate system used in the present study. We solve the unsteady two-dimensional dimensionless continuity, Navier–Stokes and energy equations defined as

Mass conservation:

$$\frac{\partial}{\partial r}(r u_r) + \frac{\partial u_\theta}{\partial \theta} = 0 \tag{1}$$

r—momentum conservation:

$$\frac{\partial u_r}{\partial t} + \frac{\partial u_r^2}{\partial r} + \frac{1}{r}\frac{\partial (u_r u_\theta)}{\partial \theta} + \frac{u_r^2 - u_\theta^2}{r} = -\frac{\partial p}{\partial r} + \frac{1}{Re}\left[\nabla^2 u_r - \frac{u_r}{r^2} - \frac{2}{r^2}\frac{\partial u_\theta}{\partial \theta}\right] + f_r \tag{2}$$

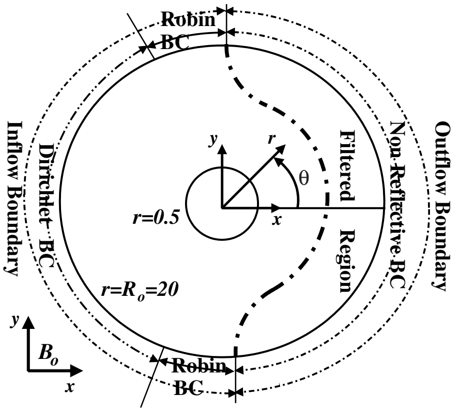

Fig. 1. Flow geometry and coordinate system along with boundary conditions.

θ—momentum conservation:

$$\frac{\partial u_\theta}{\partial t}+\frac{\partial(u_r u_\theta)}{\partial r}+\frac{1}{r}\frac{\partial u_\theta^2}{\partial\theta}+\frac{2u_r u_\theta}{r} = -\frac{1}{r}\frac{\partial p}{\partial\theta}+\frac{1}{Re}\left[\nabla^2 u_\theta-\frac{u_\theta}{r^2}+\frac{2}{r^2}\frac{\partial u_r}{\partial\theta}\right]+f_\theta \quad (3)$$

Energy conservation:

$$\frac{\partial T}{\partial t}+\frac{\partial(u_r T)}{\partial r}+\frac{1}{r}\frac{\partial(u_\theta T)}{\partial\theta} = \frac{1}{RePr}\left[\frac{1}{r}\frac{\partial}{\partial r}\left(r\frac{\partial T}{\partial r}\right)-\frac{1}{r^2}\frac{\partial^2 T}{\partial\theta^2}\right] \quad (4)$$

The dimensionless variables in the above equations are defined as

$$u_r=\frac{u_r^*}{U_\infty},\quad u_\theta=\frac{u_\theta^*}{U_\infty},\quad p=\frac{p^*}{\rho U_\infty^2},\quad t=\frac{t^*U_\infty}{D},\quad T=\frac{T^*-T_\infty}{T_s-T_\infty},\quad r=\frac{r^*}{D} \quad (5)$$

In the above equations, ρ, U_∞, T_∞, T_s, and D represent the density, free stream velocity, free stream temperature, cylinder surface temperature and cylinder diameter. The superscript * in Eq. (5) represents the dimensional variables. u_r, u_θ, T, p, t, r and θ are the non-dimensional radial velocity, circumferential velocity, temperature, pressure, time, radial direction and circumferential direction. The above non-dimensionalization results in two-dimensionless parameters: $Re = U_\infty D/\nu$ and $Pr = \nu/\alpha$, where ν and α are the kinematic viscosity and thermal diffusivity. In the simulations to be reported here the Prandtl number, Pr, has been taken to be 0.02, 0.7 and 7 corresponding to liquid metal, air and water, respectively. $Pr = 0.7$ is corresponding to air which is not electrically conducting. However, $Pr = 0.7$ is considered as just an intermediate numerical value in order to demonstrate the tendency for increasing Pr. The Reynolds number of $Re = 100$ and 200 are considered. The purpose of the present study is to investigate the effects of applied magnetic fields on the forced convection around a cylinder and as a result the effect of buoyancy is ignored in the present study. We limit attention to the case of incompressible flow of constant thermodynamic and transport property for the fluid. We also assume that the flow is two-dimensional and invariant along the spanwise direction for the low Reynolds numbers considered in the present problem.

The applied magnetic field is parallel to the x-direction with constant values and as a result the Lorentz forces f_r and f_θ acting on the fluid is defined as

$$f_r = N[u_r(\sin\theta)^2 + u_\theta\sin\theta\cos\theta] \quad (6)$$

$$f_\theta = N[u_\theta(\cos\theta)^2 + u_r\sin\theta\cos\theta] \quad (7)$$

The detailed derivation for above Eqs. (6) and (7) can be found in Mutschke et al. [24,26]. Here we can define additional dimensionless parameter called as Stuart number or interaction parameter, which is the ratio of electromagnetic force to inertia force, defined as

$$N = \sigma B_0^2 D/(\rho U_\infty) \quad (8)$$

where σ and B_0 represent electric conductivity and external magnetic field.

3. Numerical methodology

A spectral methodology is used for the spatial discretization. A spectral Chebyshev discretization is defined along r-direction. The grid points are the Gauss–Lobatto points corresponding to Chebyshev expansion and are therefore non-uniformly distributed defined as

$$r_i = -\cos\left[\frac{\pi(i-1)}{N_r-1}\right],\quad 1\leqslant i\leqslant N_r \quad (9)$$

A Fourier expansion is used along the periodic circumferential direction defined as

$$\theta_j = \frac{jL_\theta}{N_\theta},\quad 0\leqslant j\leqslant N_\theta-1,\ L_\theta = 2\pi \quad (10)$$

A two-step time-split scheme is used to advance the flow field. First the velocity is advanced from time level 'n' to an intermediate level by solving the advection-diffusion equation. In the advection-diffusion step, the non-linear terms are treated explicitly using third-order Adams–Bashforth scheme. The diffusion terms are treated implicitly using Crank–Nicolson scheme. Then a Poisson equation for pressure is solved fully implicitly. The final divergence-free velocity field at '$n+1$' is obtained with a pressure-correction step. The temperature field is advanced in a similar manner with third-order Adams–Bashforth scheme for the advection term and Crank–Nicolson scheme for the diffusion term.

In all the simulations the initial velocity field is taken to be the potential flow and the initial thermal field is taken to be uniform free stream temperature. The vortex shedding is initiated by providing a small 'conveyor-belt' type of slip velocity on the body, which varies sinusoidally for a short period of time Mittal and Balachandar [2]. On the surface of the cylinder, no-slip and no-penetration boundary conditions are enforced for the velocity field, while isothermal boundary condition ($T = 1$) is enforced for the temperature. The computational outer boundary is placed at $r = 20$ and it serves both as inflow (for $-\pi/2 \leqslant \theta \leqslant \pi/2$) and outflow (for $\pi/2 \leqslant \theta \leqslant -\pi/2$) boundary. Over the inflow section a uniform isothermal ($T = 0$) inflow is specified and at the outflow section it is important to specify a well-posed non-reflecting boundary condition capable of convecting large vortical disturbances out of the computational domain. Here we employ the buffer domain technique as described in Mittal and Balachandar [2], who tested the effectiveness of the inflow and outflow boundary conditions in detail. They showed that quantities like lift, drag and Strouhal number of vortex shedding are independent of the size of the computational domain and that the buffer domain boundary conditions allow for smooth advection of the vortical structures past the outflow boundary without any spurious reflection. The dimensionless time step used in the present calculation is 0.002 and the number of grid points used is 121×164 ($r \times \theta$) for $Re = 100$ and 151×164 ($r \times \theta$) for $Re = 200$, respectively. Grid independence of the solution has been confirmed with additional simulations on much finer grids. The computations were advanced in time until it was observed that the drag, lift and heat transfer coefficients have reached a statistically stationary state.

Once the velocity and temperature fields are obtained, the local, surface-averaged, time-averaged, and time and surface-averaged Nusselt number are defined as

$$Nu = \left.\frac{\partial \theta}{\partial n}\right|_{\text{wall}} \quad \langle Nu \rangle = \frac{1}{W}\int_0^W Nu\,\mathrm{d}S \quad \overline{Nu} = \frac{1}{t_{\mathrm{p}}}\int_0^{t_{\mathrm{p}}} Nu\,\mathrm{d}t$$

$$\langle \overline{Nu} \rangle = \frac{1}{t_{\mathrm{p}}}\int_0^{t_{\mathrm{p}}} \langle Nu \rangle\,\mathrm{d}t \tag{11}$$

where n is the normal direction to the walls, W is the cylinder surface and t_{p} is the period of time integration.

4. Results and discussion

4.1. Fluid flow

Fig. 2 shows the distribution of instantaneous vorticity for different Stuart numbers of $N = 0$, 0.1 and 0.2 at the Reynolds number of 100. When $N = 0$ corresponding to the case without applied magnetic fields, the flow is time-dependent and we can observe the vortex shedding in the wake. If the magnetic fields are applied to the cross flow over a cylinder, the vertical force acts to the negative y-direction at the upper part of centerline ($x = 0$) and to the positive y-direction at the lower part. This vertical force caused by the magnetic fields increases the resistance for the cross flow over a cylinder. As a result, when $N = 0.1$, the boundary layer thickness formed on the cylinder surface increases and the vortex street formed in the wake region is elongated in the streamwise direction with decreasing vortex strength. The flow is still time-dependent at the Stuart number of $N = 0.1$. If the Stuart number is increased further to 0.2, the flow is stabilized and changes its distribution from the time-dependent pattern with vortex shedding in the wake at $N = 0$ and 0.1 to the steady state with a symmetric shape along the centerline ($x = 0$).

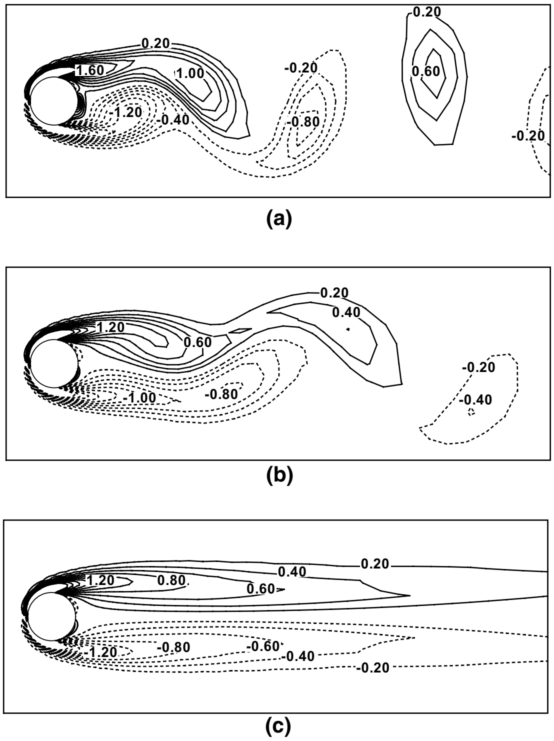

Fig. 2. Instantaneous vorticity contours at (a) $N = 0$, (b) $N = 0.1$ and (c) $N = 0.2$ for $Re = 100$.

Fig. 3 shows the time history of lift coefficient for the Reynolds number of 100. The time history of C_{L} during the dimensionless time of $175 \leqslant t \leqslant 200$ corresponds to the case without applied magnetic fields ($N = 0$). The flow field at $t = 200$ for the case of $N = 0$ is used as an initial condition to calculate the fluid flow in the presence of applied magnetic fields. If we apply the magnetic field at $N = 0.06$ corresponding to the case with relatively weak magnetic strength, the period of C_{L} becomes

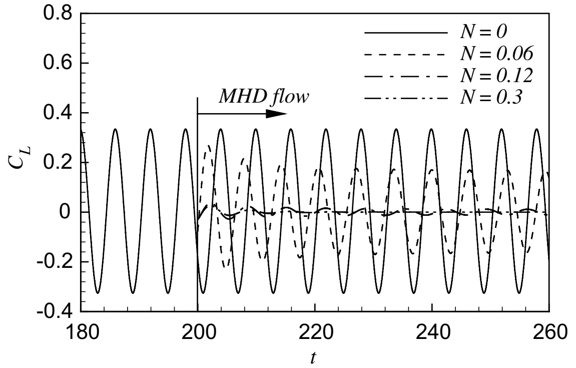

Fig. 3. Time history of lift coefficients for different Stuart numbers at $Re = 100$.

larger with decreasing oscillating amplitude as time goes on, compared to the case without the applied magnetic fields. C_L still maintains its time-dependent oscillating pattern at $N = 0.06$. However, if N is further increased to 0.3, the oscillating amplitude of C_L decreases very rapidly and C_L approaches to zero at the dimensionless time of $t > 210$, corresponding to ten-dimensionless time later after the magnetic field is applied to the flow field at $t = 200$. Thus the flow becomes steady at the dimensionless time of $t > 210$ for $N = 0.3$.

Fig. 4 shows the Strouhal number variation as a function of Stuart number at the Reynolds number of 100. As shown in Fig. 3, an oscillating period of C_L increases with increasing N corresponding to the increasing magnetic field intensity. As a result the Strouhal number decreases almost linearly with increasing N, which is another evidence to prove that the flow is stabilized as the magnitude of applied magnetic fields increases.

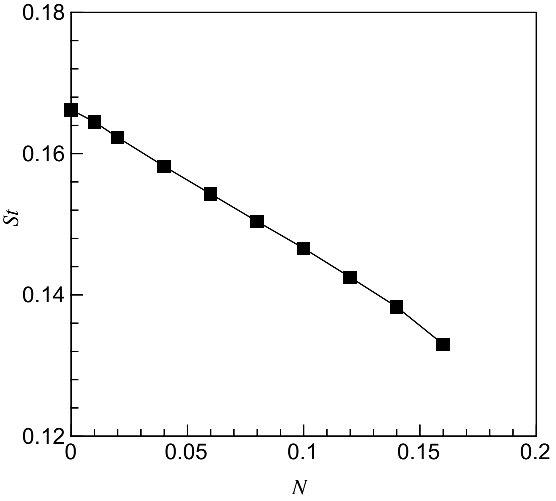

Fig. 4. Variation of Strouhal number as a function of Stuart number at $Re = 100$.

Fig. 5 shows the time-averaged wall vorticity ($\overline{\omega_w}$) as a function of circumferential direction θ for different Stuart numbers at the Reynolds number of 100. Here, overbar—denotes the time-averaged quantity. Here $\theta = 0°$ and $180°$ represent the rear and front stagnation points as shown in Fig. 1. When $0 \leqslant N < N_{cr}$, the flow past a cylinder is time-dependent, and time-averaged wall vorticity around the top and bottom parts of cylinder ($\theta \sim 130°$ and $230°$) decreases with increasing N as shown in Fig. 5(a), because the boundary layer thickness

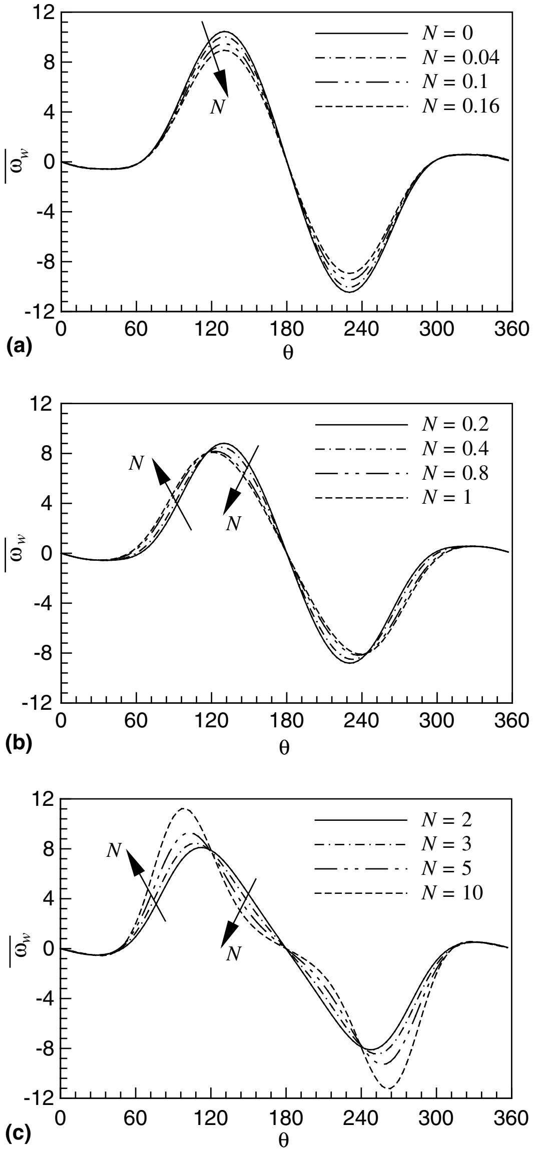

Fig. 5. Time-averaged wall vorticity as a function of θ for (a) $0 \leqslant N \leqslant 0.16$, (b) $0.2 \leqslant N \leqslant 1$ and (c) $2 \leqslant N \leqslant 10$ at $Re = 100$.

and gradient of circumferential velocity increase due to increasing flow resistance to the cross flow over a cylinder. Here N_{cr} is a value of the Stuart number, at which the flow changes its pattern from the time-dependent to the steady state, depending on the Reynolds number. N_{cr} is 0.18 at $Re = 100$ and 0.3 at $Re = 200$, respectively. When $N_{cr} < N \leqslant 1$, the wall vorticity at the upstream region from the front stagnation point of $\theta = 180°$ to $\theta \sim 116°$ (and $\theta \sim 244°$) keeps decreasing similar to the case when $0 \leqslant N < N_{cr}$, because the velocity boundary layer thickness increases owing to increasing flow resistance with increasing N. However, the wall vorticity at the downstream region from $\theta \sim 116°$ (and $\theta \sim 244°$) to the separation point increases as N increases at $N_{cr} < N \leqslant 1$, because the flow is squeezed by the vertical force acting on the cylinder, the vortex street is elongated more in the streamwise direction and the thickness of velocity boundary layer decreases. The circumferential location, $\theta_{\overline{\varpi}_{w,max}}$, at which the wall vorticity $\overline{\varpi_w}$ has a maximum value, is still at the upstream region when $N_{cr} < N \leqslant 1$. If the Stuart number is increased further to $2 \leqslant N \leqslant 10$, the wall vorticity decreases at the upstream region from the front stagnation point to $\theta \sim 120°$ (and $\theta \sim 240°$) and increases at the downstream region from $\theta \sim 120°$ (and $\theta \sim 240°$) to the separation point with increasing N, similar to the case when $N_{cr} < N \leqslant 1$. However, as N increases in the range of $2 \leqslant N \leqslant 10$, the location of $\theta_{\overline{\varpi}_{w,max}}$ moves to the downstream region from the upstream region at $N_{cr} < N \leqslant 1$, because the squeezing effect caused by the vertical force in the presence of magnetic fields increases with increasing N. The change of wall vorticity in the wake region from the separation point to the rear stagnation point for different Stuart numbers is very small.

Fig. 6 shows the time-averaged separation angle as a function of Stuart number at the Reynolds numbers of 100 and 200. When the flow is time-dependent with relatively weak strength of applied magnetic field, the separation angle increases slightly, meaning that the separation point moves slightly to the upstream direction due to increasing velocity boundary layer thickness with increasing N. The change in the separation angle is very small when the strength of applied magnetic fields is relatively weak. However, if the Stuart number is increased further, the flow becomes steady, the separation angle decreases and the separation point moves to the downstream direction, due to increasing squeezing effects with increasing N. The change in the separation angle is relatively large when the strength of applied magnetic fields is strong, compared to the small change in the separation angle when the strength of applied magnetic fields is weak. The present calculation results for the separation angle as a function of Stuart number at $Re = 200$ agree well with the computational results obtained by Mutschke et al. [26] to show the validity of present calculation.

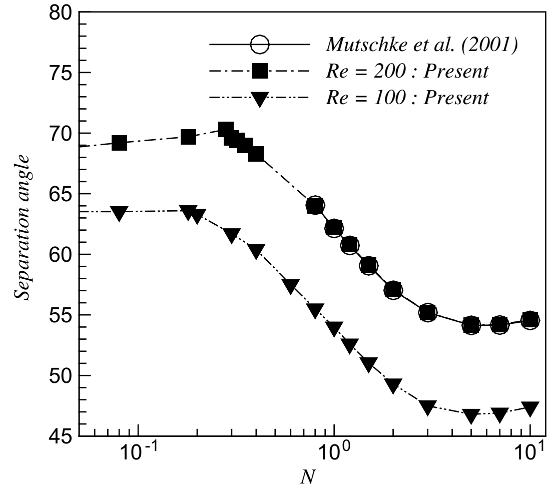

Fig. 6. Time-averaged separation angle as a function of Stuart number at $Re = 100$ and 200.

Fig. 7 shows the time-averaged pressure coefficient ($\overline{C_P}$) as a function of circumferential direction θ for different Stuart numbers at the Reynolds number of 100. The value of $\overline{C_P}$ at the front stagnation point of $\theta = 0$ does not depend on the strength of applied magnetic fields and has a constant value of 1. This means that all the momentum of free stream is converted to the pressure at the front stagnation point, irrespective of the cases with and without applied magnetic fields. The value of $\overline{C_P}$ for different Stuart numbers decreases in the favorable pressure gradient region, reaches a minimum value in the zero pressure gradient region and increases in the adverse pressure gradient region. Pressure distribution along the surface has a deep relation with the wall vorticity distribution. If the velocity gradient of

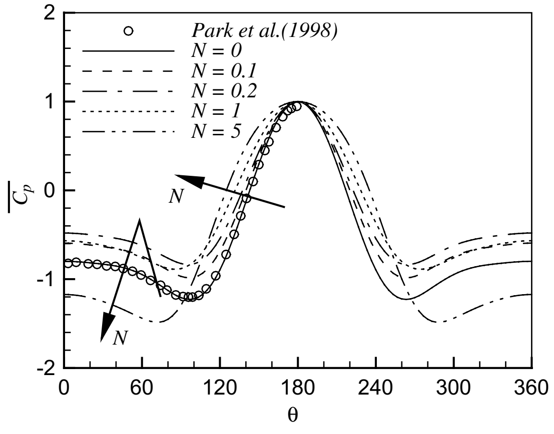

Fig. 7. Time-averaged pressure coefficient as a function of θ for different Stuart numbers at $Re = 100$.

circumferential velocity and wall vorticity increase, the absolute pressure gradient in the circumferential direction also increases, resulting in increasing pressure difference between the stagnation and θ points. When the Stuart number increases in the range of $0 \leqslant N \leqslant 0.2$, the wall vorticity in the favorable pressure gradient decreases and as a result $\overline{C_\mathrm{P}}$ increases in the whole region on the cylinder surface with increasing N. When the Stuart number is increased to 1 and 5, the wall vorticity at the upstream of favorable pressure gradient region is smaller than that at $N = 0.2$, whereas the wall vorticity at the downstream for $N = 1$ and 5 is larger than that for $N = 0.2$, as shown in Fig. 5(b) and (c). Thus, $\overline{C_\mathrm{P}}$ at the upstream of favorable pressure gradient region for $N = 1$ and 5 is larger than that for $N = 0.2$, whereas $\overline{C_\mathrm{P}}$ at the downstream of favorable pressure gradient region and at the adverse pressure gradient region for $N = 1$ and 5 is smaller than that for $N = 0.2$. The value of $\overline{C_\mathrm{P}}$ in the adverse pressure gradient region for $N = 5$ is much smaller than that for $N = 0$, 0.1, 0.2 and 1, due to the strong effect of magnetic field on the flow past a circular cylinder. The present results for $\overline{C_\mathrm{P}}$ distribution for $N = 0$ agree very well with the calculation results obtained by Park et al. [27] to show another validity of present calculation.

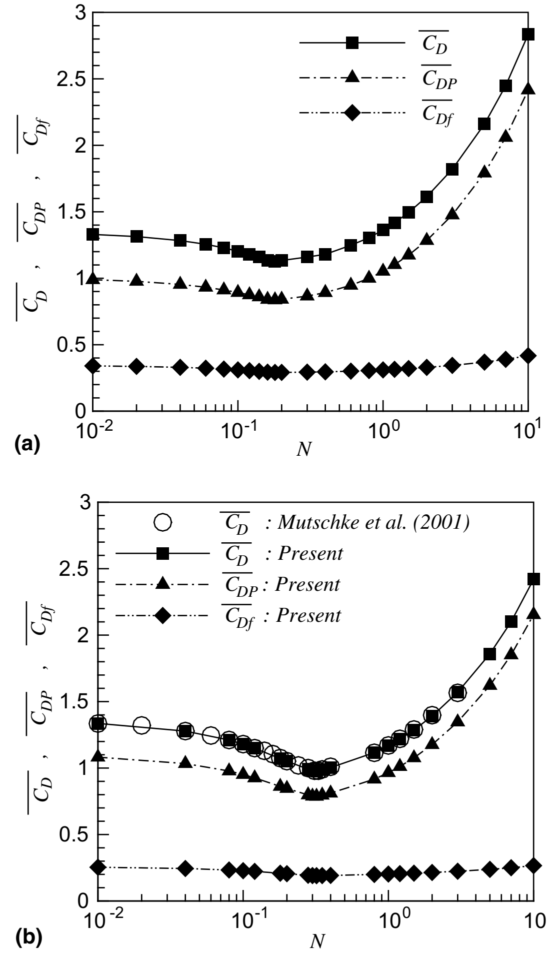

Fig. 8. Time-averaged drag coefficients as a function of Stuart number at (a) $Re = 100$ and (b) $Re = 200$.

Fig. 8 shows time-averaged drag coefficient ($\overline{C_\mathrm{D}}$) as a function of Stuart number (N) for different Reynolds numbers of 100 and 200. The drag coefficient ($\overline{C_\mathrm{D}}$) consists of the sum of pressure drag coefficient ($\overline{C_\mathrm{Dp}}$) and friction drag coefficient ($\overline{C_\mathrm{Df}}$). If $N < N_\mathrm{cr}$, the pressure and $\overline{C_\mathrm{P}}$ in the wake (corresponding to the adverse pressure gradient region) increases with increasing N as shown in Fig. 7. As a result $\overline{C_\mathrm{Dp}}$ and $\overline{C_\mathrm{D}}$ decrease slightly with increasing N when $N < N_\mathrm{cr}$. If the Stuart number increases at $N > N_\mathrm{cr}$, $\overline{C_\mathrm{P}}$ in the wake decreases and as a result $\overline{C_\mathrm{D}}$ increases very rapidly. When the Reynolds number is 100, $\overline{C_\mathrm{D}}$ has a minimum value at $N = N_\mathrm{cr}$ (where $N_\mathrm{cr} = 0.18$). The minimum value of $\overline{C_\mathrm{D}}$ is 1.128, which is 16% less than the value of $\overline{C_\mathrm{D}}$ corresponding to the case without applied magnetic field ($N = 0$). If the Reynolds number is increased to 200, the minimum value of $\overline{C_\mathrm{D}}$ at $N = N_\mathrm{cr}$ (where $N_\mathrm{cr} = 0.3$) is 0.98, which is a decrease of 26% compared with the value of $\overline{C_\mathrm{D}}$ for the case of $N = 0$. The present calculation results for $\overline{C_\mathrm{D}}$ are compared with the computational results obtained by Mutschke et al. [26] as shown in Fig. 8(b). The agreement between two results is very good.

Fig. 9 shows the maximum value of total, pressure and friction lift coefficients as a function of Stuart number for the Reynolds number of 100. Here the maximum value of lift coefficients corresponds to the amplitude of oscillating lift coefficients after they reach a quasi-steady state. If the applied magnetic fields increase

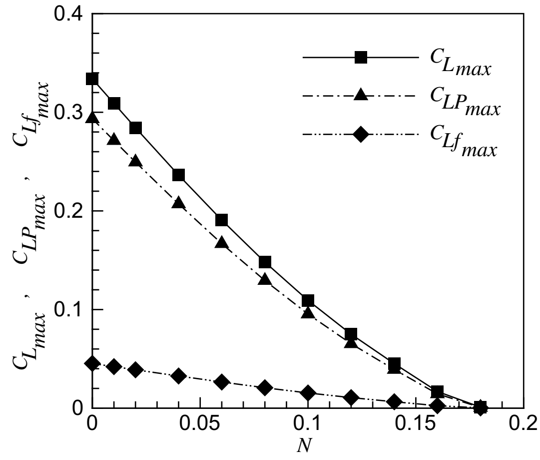

Fig. 9. Maximum lift coefficients as a function of Stuart number at $Re = 100$.

with increasing Stuart number, the Lorentz force acting on the flow past a circular cylinder to the cross streamwise (y) direction becomes larger and makes the strength of vortex in the wake weaker. As a result, the lift coefficients keeps decreasing with increasing Stuart number and become zero when $N > N_{\mathrm{cr}}$. This result represents that, when $N < N_{\mathrm{cr}}$, the flow without and with applied magnetic fields is time-dependent. However, if the Stuart number increases at $N > N_{\mathrm{cr}}$, the flow in the presence of applied magnetic fields changes its distribution to the steady state.

4.2. Heat transfer

Figs. 10–12 show the distribution of instantaneous dimensionless temperature fields for different Stuart numbers of $N = 0$, 0.1 and 0.2 and different Prandtl numbers of $Pr = 0.02$, 0.7 and 7 at $Re = 100$. When the Prandtl number increases from 0.02 to 7, the thickness of thermal boundary layer decreases and as a result the temperature gradient (heat transfer rate) around a cylinder increases. When $N < N_{\mathrm{cr}}$, the temperature fields are time-dependent and show shedding phenomena in the wake, because the flow is time-dependent at these Stuart numbers. When $Pr = 0.02$, the unsteadiness is very weak, because the thickness of thermal boundary layer is much larger than that of velocity boundary layer and as a result the temperature boundary layer is not much affected by the velocity boundary layer. If the Prandtl number is increased to 0.7 and 7 at $N < N_{\mathrm{cr}}$, the temperature fields follows the flow fields and the unsteadiness becomes larger due to decreasing thermal boundary layer thickness with increasing Prandtl number. When $N > N_{\mathrm{cr}}$, the temperature fields become a steady state for different Prandtl numbers of $Pr = 0.02$, 0.7 and 7, because the flow is not time-dependent.

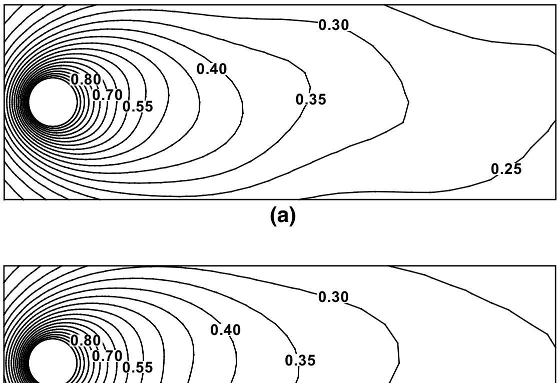

Fig. 10. Instantaneous temperature contours for different Stuart numbers of (a) $N = 0$, (b) $N = 0.1$ and (c) $N = 0.2$ at $Re = 100$ and $Pr = 0.02$.

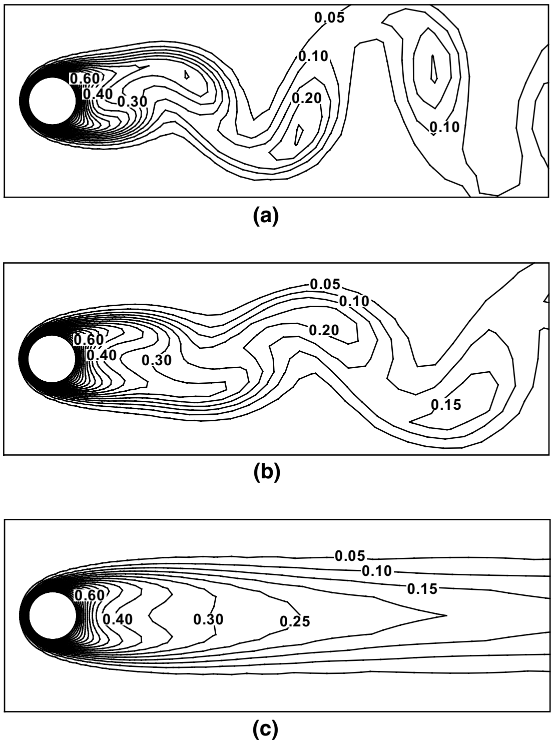

Fig. 11. Instantaneous temperature contours for different Stuart numbers of (a) $N = 0$, (b) $N = 0.1$ and (c) $N = 0.2$ at $Re = 100$ and $Pr = 0.7$.

Fig. 13 shows the time-averaged local Nusselt number, $\overline{Nu}$, as a function of circumferential direction θ for different Stuart numbers at $Re = 100$ and $Pr = 0.02$. The distribution of $\overline{Nu}$ has a deep relation with wall vorticity distribution shown in Fig. 5. If the wall vorticity increases with increasing N, the thermal boundary layer thickness decreases and as a result $\overline{Nu}$ increases. The opposite is also true. As N increases in the range of $0 \leqslant N < N_{\mathrm{cr}}$, the wall vorticity decreases and as a result $\overline{Nu}$ decreases. However, as N increases in the range of $N_{\mathrm{cr}} < N \leqslant 1$, the wall vorticity decreases at $116° \leqslant \theta \leqslant 180°$ (and $180° \leqslant \theta \leqslant 244°$) and increases at $0° \leqslant \theta \leqslant 116°$ (and $244° \leqslant \theta \leqslant 360°$), as shown in Fig. 5(b).

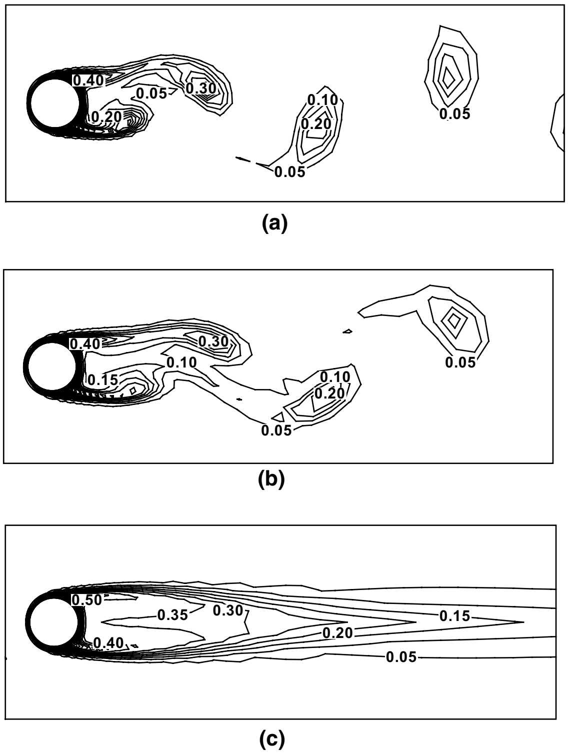

Fig. 12. Instantaneous temperature contours for different Stuart numbers of (a) $N = 0$, (b) $N = 0.1$ and (c) $N = 0.2$ at $Re = 100$ and $Pr = 7$.

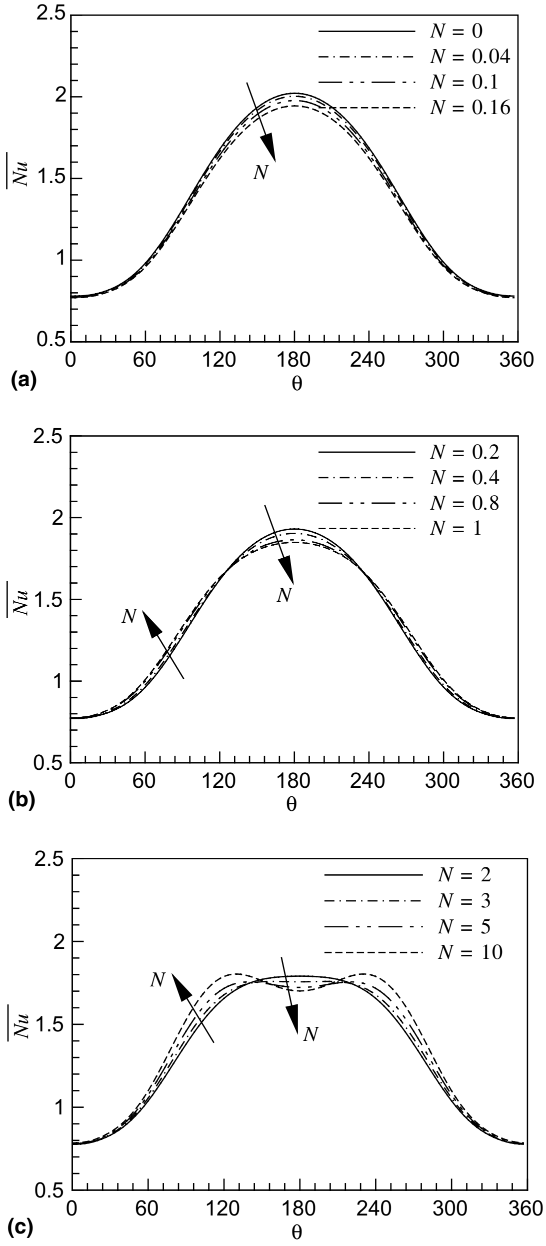

Fig. 13. Time-averaged local Nusselt number as a function of θ for (a) $0 \leqslant N \leqslant 0.16$, (b) $0.2 \leqslant N \leqslant 1$ and (c) $2 \leqslant N \leqslant 10$ at $Re = 100$ and $Pr = 0.02$.

Thus $\overline{Nu}$ decreases around the front stagnation point ($144° \leqslant \theta \leqslant 216°$) and increases at the downstream ($0° \leqslant \theta \leqslant 144°$ and $216° \leqslant \theta \leqslant 360°$), as N increases in the range of $N_{\mathrm{cr}} < N \leqslant 1$ as shown in Fig. 13(b). When $0 \leqslant N \leqslant 1$, $\overline{Nu}$ has a maximum value at the front stagnation point of $\theta = 180°$ and decreases as we move in the streamwise direction from the front stagnation to the rear stagnation point, irrespective of the magnitude of the applied magnetic fields. If N is increased further to $2 \leqslant N \leqslant 10$, the distribution of $\overline{Nu}$ as a function of θ shows the similar pattern to the case of $N_{\mathrm{cr}} < N \leqslant 1$, giving decreasing $\overline{Nu}$ around the front stagnation point and increasing $\overline{Nu}$ at the downstream as N increases. However, the circumferential location, $\theta_{\overline{Nu}_{\max}}$, at which $\overline{Nu}$ has a maximum value, moves from the front stagnation point at $0 \leqslant N \leqslant 1$ to the downstream direction at $2 \leqslant N \leqslant 10$.

Figs. 14 and 15 show the time-averaged local Nusselt number, $\overline{Nu}$, as a function of circumferential direction θ for different Stuart numbers at $Pr = 0.7$ and 7, respectively. The Reynolds number used is 100. The thickness of velocity boundary layer does not depend on the Prandtl number variation. However, the thickness of thermal boundary layer decreases with increasing Prandtl number. Thus, in the absence of applied magnetic field ($N = 0$), the distribution of $\overline{Nu}$ from the front stagnation ($\theta = 180°$) to the separation points for different Prandtl numbers of 0.02, 0.7 and 7 has a generally similar shape, showing that $\overline{Nu}$ has a maximum value at the front stagnation point and decrease as we move from the stagnation to separation point. When $Pr = 0.02$ at $N = 0$, $\overline{Nu}$ keep decreasing as we move from the

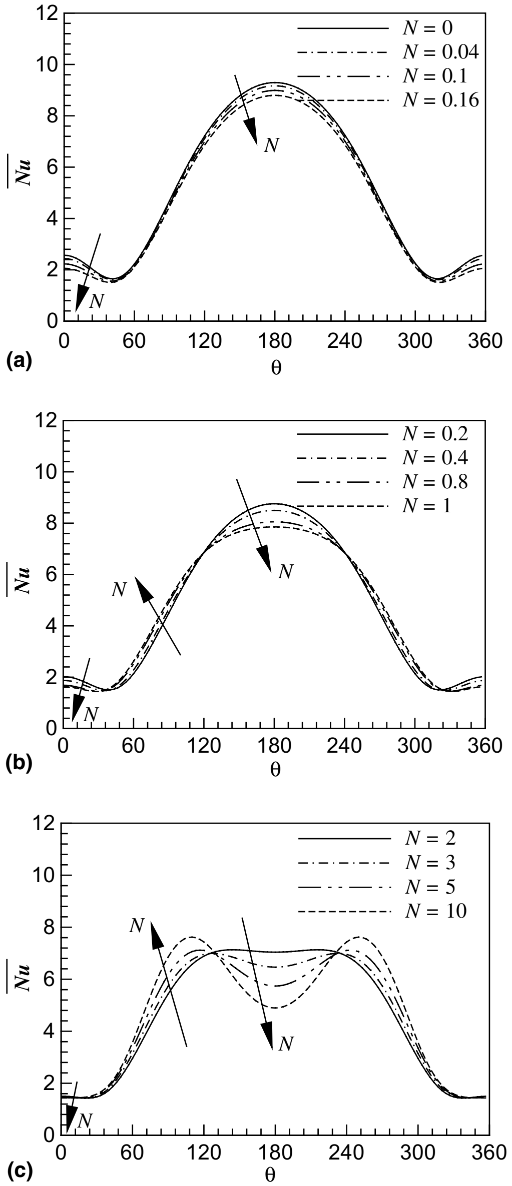

Fig. 14. Time-averaged local Nusselt number as a function of θ for (a) $0 \leqslant N \leqslant 0.16$, (b) $0.2 \leqslant N \leqslant 1$ and (c) $2 \leqslant N \leqslant 10$ at $Re = 100$ and $Pr = 0.7$.

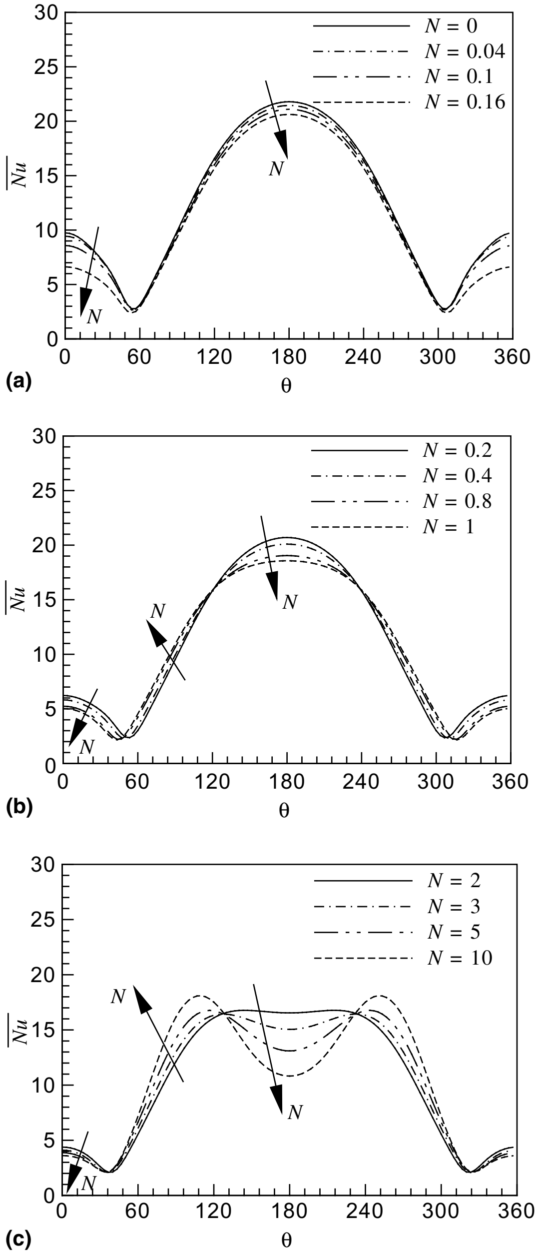

Fig. 15. Time-averaged local Nusselt number as a function of θ for (a) $0 \leqslant N \leqslant 0.16$, (b) $0.2 \leqslant N \leqslant 1$ and (c) $2 \leqslant N \leqslant 10$ at $Re = 100$ and $Pr = 7$.

separation to rear stagnation points. However, if the Prandtl number is increased to 0.7 and 7 at $N = 0$, $\overline{Nu}$ has a minimum value around the separation point and increase as we move from the separation to rear stagnation point due to the mixing effect in the wake region. The value of $\overline{Nu}$ in the wake region at $N = 0$ for $Pr = 7$ increases more rapidly than that for $Pr = 0.7$, because the thermal boundary layer becomes much smaller than the velocity boundary layer and responds very quickly to the variation of velocity boundary layer as the Prandtl number increases. If we apply the magnetic field, the variation of $\overline{Nu}$ for different N from the front stagnation to the separation point at $Pr = 0.7$ and 7 is generally similar to that at $Pr = 0.02$. As N increases at $Pr = 0.7$ and 7, $\overline{Nu}$ increases around the locations, where the wall vorticity increases, whereas $\overline{Nu}$ decreases around the locations where the wall vorticity decreases. However, as the Prandtl number increases, the extent of variation in $\overline{Nu}$ for different N becomes larger as shown in Figs. 14 and 15, because the temperature fields respond more quickly to the variation of flow fields. When $Pr = 0.02$, the distribution of $\overline{Nu}$ in the wake region does not depend on the variation of N. However, as N increases at the Prandtl numbers of 0.7 and 7, the value of $\overline{Nu}$ in the wake region decreases, because the size of wake decreases due to the movement of separation point to the downstream direction as shown in Fig. 6.

Fig. 16(a) shows the time and surface-averaged Nusselt number, $\langle\overline{Nu}\rangle$, as a function of Stuart number N at $Re = 100$ and $Pr = 0.02$. The variation of $\langle\overline{Nu}\rangle$ shows different behavior at different sections of N, because the flow and temperature fields have different distribution depending on N. When $N < N_{\mathrm{cr}}$ where $N_{\mathrm{cr}} = 0.18$, the flow and temperature are time-dependent and the local Nusselt number $\overline{Nu}$ in Fig. 13 decreases as N increases. The value of $\langle\overline{Nu}\rangle$ decreases slowly as N increases in the range of weak applied magnetic fields around $N = 0$. However, the decreasing rate of $\langle\overline{Nu}\rangle$ increases gradually as N increases further in the range of $N < N_{\mathrm{cr}}$. As a result $\langle\overline{Nu}\rangle$ has a parabolic shape at $N < N_{\mathrm{cr}}$. The value of $\langle\overline{Nu}\rangle$ has a minimum value of 1.31 around $N = N_{\mathrm{cr}}$, which is 3% less than the value of $\langle\overline{Nu}\rangle$ at $N = 0$. However, if $N > N_{\mathrm{cr}}$, the flow and temperature fields becomes a steady state. As N increases at $N > N_{\mathrm{cr}}$, $\langle\overline{Nu}\rangle$ increases because the increasing rate of local Nusselt number $\overline{Nu}$ at the downstream region is larger than the decreasing rate of $\overline{Nu}$ around a front stagnation point.

Fig. 16(b) and (c) show the time and surface-averaged Nusselt number, $\langle\overline{Nu}\rangle$, as a function of Stuart number N for different Prandtl numbers of 0.7 and 7 at $Re = 100$. As the Prandtl number increases, the thermal boundary layer thickness decreases as previously explained and as a result $\langle\overline{Nu}\rangle$ increases. When $N < N_{\mathrm{cr}}$, the distribution of $\langle\overline{Nu}\rangle$ for $Pr = 0.7$ and 7 shows a similar parabolic shape to that for $Pr = 0.02$. However, as N increases in the range of $N_{\mathrm{cr}} < N < N_{\langle\overline{Nu}\rangle_{\min}}$ where $N_{\langle\overline{Nu}\rangle_{\min}}$ is the Stuart number at which the $\langle\overline{Nu}\rangle$ has a minimum value, the value of $\langle\overline{Nu}\rangle$ for $Pr = 0.7$ and 7 keeps decreasing, unlike to the case for $Pr = 0.02$, because the increasing rate of $\overline{Nu}$ at the downstream region is smaller than the decreasing rate of $\overline{Nu}$ around a front stagnation point and in the wake region. As N increases in the range of $N \geqslant N_{\langle\overline{Nu}\rangle_{\min}}$, $\langle\overline{Nu}\rangle$ increases, because the increasing rate of $\overline{Nu}$ at the downstream region becomes larger than the decreasing rate of $\overline{Nu}$ around a front stagnation point and in the wake region. When $Pr = 0.7$, $N_{\langle\overline{Nu}\rangle_{\min}}$ is about 3 and $\langle\overline{Nu}\rangle_{\min}$ is 4.8, which is 8.6% less than that corresponding to the case without applied magnetic field ($N = 0$). When $Pr = 7$, $N_{\langle\overline{Nu}\rangle_{\min}}$ is about 5 and $\langle\overline{Nu}\rangle_{\min}$ is 10.5, which is 14% less than that for $N = 0$.

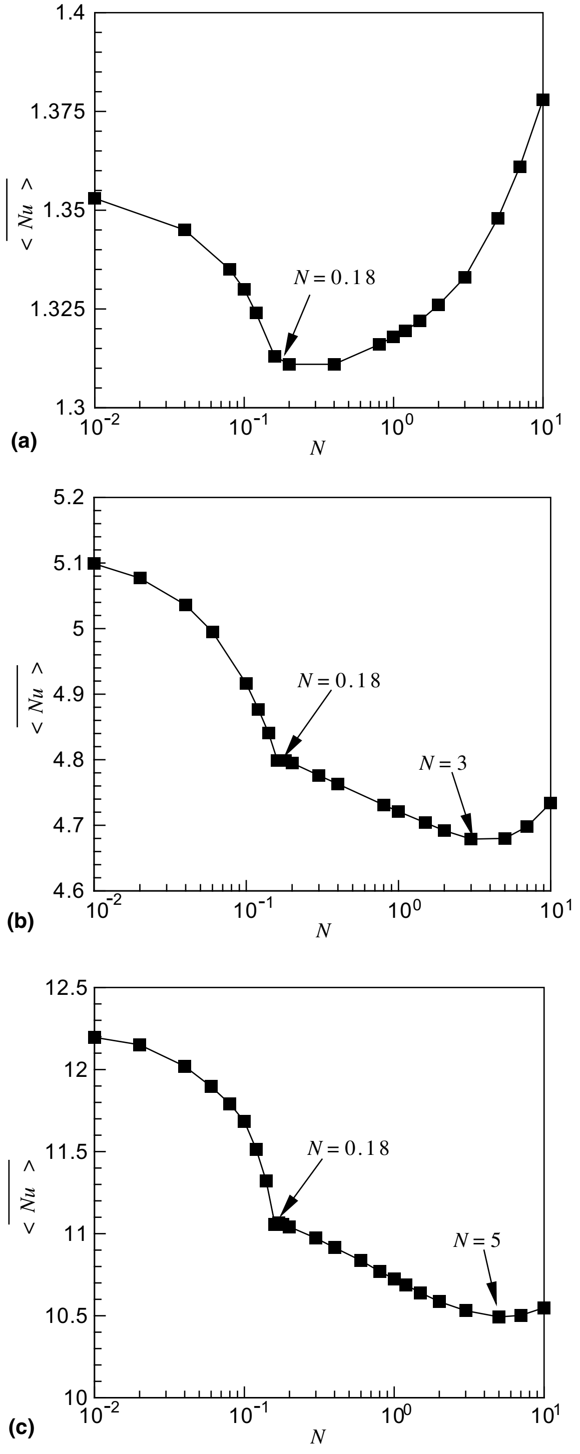

Fig. 16. Time and surface-averaged Nusselt number as a function of Stuart number of (a) $Pr = 0.02$ (b) $Pr = 0.7$ (c) $Pr = 7.0$ at $Re = 100$.

5. Conclusions

The present study numerically investigates the characteristics of two-dimensional laminar flow and heat transfer past a circular cylinder in an aligned magnetic field using the spectral method. Numerical simulations to calculate the flow and thermal fields over a cylinder are carried out for different Reynolds and Prandtl numbers in the presence of aligned applied magnetic fields. The results with the applied magnetic fields are compared with those without magnetic fields in order to investigate the effects of applied magnetic fields on the fluid flow and heat transfer characteristics past a cylinder.

When the uniform magnetic fields aligned with the free stream are applied to the flow past a circular cylinder, the Lorentz force acting on the flow damps the flow oscillation caused by the vortex shedding. As a result, wake oscillation are first weakened, eventually resulting in a steady flow with two narrow and elongated eddies. There exists the critical Stuart number N_{cr}, which makes the time-dependent fluid flow and temperature fields steady, depending on the Reynolds number.

As the Stuart number increases in the range of $N < N_{cr}$, the flow and temperature fields are time-dependent and their oscillating amplitude decreases, resulting in decreasing Strouhal number and lift coefficients. The distribution of time-averaged pressure and drag coefficients and Nusselt number has a deep relation with that of wall vorticity along the cylinder surface. Because the wall vorticity along the cylinder surface decreases with increasing Stuart number at $N < N_{cr}$, the time-averaged pressure coefficient, time-averaged local Nusselt number, and time and surface-averaged Nusselt number increase whereas the time-averaged drag coefficient decreases. The time-averaged separation point moves slightly to the upwards with increasing Stuart number at $N < N_{cr}$.

As the Stuart number increases further in the range of $N > N_{cr}$, the flow and temperature fields becomes a steady state. The wall vorticity decreases around the front stagnation point and increases at the downstream region with increasing Stuart number. As a result, as the Stuart number increases at $N > N_{cr}$, the time-averaged pressure coefficient increases at the upstream and decreases around the wake region, and the time-averaged drag coefficient increase. The separation point moves to the downstream direction and as a result the size of wake decreases with increasing Strouhal number at $N > N_{cr}$. The time-averaged local Nusselt number decreases around the front stagnation point and in the wake region with increasing Strouhal number at $N > N_{cr}$ and increases at the downstream region before the separation point. The extent of variation in the time-averaged local Nusselt number along the cylinder surface for different Stuart numbers becomes larger as the Prandtl number increases. The time and surface-averaged Nusselt number has a minimum value at $N = N_{cr}$ when $Pr = 0.02$. However, if the Prandtl number increases to 0.7 and 7, the Stuart numbers, at which the time and surface-averaged Nusselt number has a maximum value, become larger than N_{cr}.

Acknowledgements

This work was supported by Advanced Ship Engineering Research Center (ASERC) of Pusan National University through Korea Science and Engineering Foundation.

References

[1] M. Braza, P. Chassaing, H.H. Minh, Numerical study and physical analysis of the pressure and velocity fields in the near wake of a circular cylinder, J. Fluid Mech. 165 (1986) 79–130.

[2] R. Mittal, S. Balachandar, Direct numerical simulation of flow past elliptic cylinders, J. Comput. Phys. 124 (1994) 351–367.

[3] C.H.K. Williamson, Oblique and parallel modes of vortex shedding in the wake of a circular cylinder at low Reynolds numbers, J. Fluid Mech. 206 (1989) 579–628.

[4] P.K. Stansby, The effects of end plates on the base pressure coefficient of a circular cylinder, J. Aerosp. Sci. 78 (1974) 36–37.

[5] A. Roshko, On the wake and drag of bluff bodies, J. Aerosp. Sci. 22 (1955) 124–132.

[6] M.F. Unal, D. Rockwell, On vortex formation from a cylinder. Part 2. Control by splitter-plate interference, J. Fluid Mech. 190 (1987) 513–529.

[7] J.H. Gerrard, The mechanics of the formation region of vortices behind bluff bodies, J. Fluid Mech. 25 (1966) 401–413.

[8] K.Y. Kwon, H.C. Choi, Control of laminar vortex shedding behind a circular cylinder using splitter plates, Phys. Fluids 8 (1996) 479–486.

[9] M. Gaster, Vortex shedding from slender cones at low Reynolds numbers, J. Fluid Mech. 38 (1969) 565–576.

[10] D. Gerich, H. Eckelmann, Influence of end plate and free ends on the shedding frequency of circular cylinders, J. Fluid Mech. 122 (1982) 109–121.

[11] F.H. Shair, A.S. Grove, E.E. Petersen, A. Acrivos, The effect of confining walls on the stability of the steady wake behind a circular cylinder, J. Fluid Mech. 17 (1963) 546–550.

[12] C.J. Wood, The effect of base bleed on a periodic wake, J. R. Aeronaut. Soc. 68 (1964) 477–482.

[13] P.W. Bearman, The effect of base bleed on the flow behind a twodimensional model with a blunt trailing edge, Aeros. Q. 18 (1967) 207–225.

[14] M. Schumm, E. Berger, P.A. Monkewitz, Self-excited oscillations in the wake of two-dimensional bluff bodies and their control, J. Fluid Mech. 271 (1994) 10–50.

[15] P.J. Strykowski, K.R. Sreenivasan, On the formation and suppression of vortex 'shedding' at low Reynolds numbers, J. Fluid Mech. 218 (1990) 71–107.

[16] K. Roussopoulos, Feedback control of vortex shedding at low Reynolds numbers, J. Fluid Mech. 248 (1993) 267–296.

[17] D.S. Park, D.M. Ladd, E.W. Hendricks, Feedback control of von Karman vortex shedding behind a circular cylinder at low Reynolds number, Phys. Fluids 6 (1994) 2390–2405.

[18] P.T. Tokumaru, P.E. Dimotakis, Rotary oscillation control of a cylinder wake, J. Fluid Mech. 224 (1991) 77–90.

[19] S.J. Baek, H.J. Sung, Numerical simulation of he flow behind a rotary oscillating circular cylinder, Phys. Fluids 10 (1998) 869–876.

[20] S.M. Kang, H.C. Choi, S.S. Lee, Laminar flow past a rotating circular cylinder, Phys. Fluids 11 (1999) 3312–3321.

[21] S. Choi, H. Choi, S. Kang, Characteristics of flow over a rotationally oscillating cylinder at low Reynolds number, Phys. Fluids 14 (2002) 2767–2777.

[22] J. Lahjomri, P. Caperan, A. Alemany, The cylinder wake in a magnetic field aligned with the velocity, J. Fluid Mech. 253 (1993) 421–448.

[23] V. Shatrov, G. Mutschke, G. Gerbeth, Numerical simulation of the two-dimensional MHD-flow around a circular cylinder, Magnetohydrodynamics 33 (1997) 5–15.

[24] G. Mutschke, G. Gerbeth, V. Shatrov, A. Tomboulides, Two- and three dimensional instabilities of the cylinder wake in an external magnetic field, Phys. Fluids 9 (1997) 3114–3116.

[25] G. Mutschke, G. Gerbeth, V. Shatrov, Cylinder wake control by magnetic field in liquid metal flows, Exp. Therm. Fluid Sci. 16 (1998) 92–99.

[26] G. Mutschke, G. Gerbeth, V. Shatrov, A. Tomboulides, The scenario of three dimensional instabilities of the cylinder wake in an external magnetic field: a linear stability analysis, Phys. Fluids 13 (2001) 723–734.

[27] J. Park, K. Kwon, H. Choi, Numerical solutions of flow past a circular cylinder at Reynolds number up to 160, KSME Int. J. 12 (1998) 1200–1205.